crystals

MDPI

Article

Combining Nanofocused X-Rays with Electrical Measurements at the NanoMAX Beamline

Lert Chayanun [1,*], Susanna Hammarberg [1], Hanna Dierks [1], Gaute Otnes [2], Alexander Björling [3], Magnus T Borgström [2] and Jesper Wallentin [1]

1 Synchrotron radiation research and NanoLund, Lund University, Lund 22100, Sweden
2 Solid state physics and NanoLund, Lund University, Lund 22100, Sweden
3 MAX IV laboratory, Lund University, Lund 22100, Sweden
* Correspondence: lert.chayanun@sljus.lu.se; Tel.: +46-76-774-2623

Received: 3 July 2019; Accepted: 15 August 2019; Published: 20 August 2019

Abstract: The advent of nanofocused X-ray beams has allowed the study of single nanocrystals and complete nanoscale devices in a nondestructive manner, using techniques such as scanning transmission X-ray microscopy (STXM), X-ray fluorescence (XRF) and X-ray diffraction (XRD). Further insight into semiconductor devices can be achieved by combining these techniques with simultaneous electrical measurements. Here, we present a system for electrical biasing and current measurement of single nanostructure devices, which has been developed for the NanoMAX beamline at the fourth-generation synchrotron, MAX IV, Sweden. The system was tested on single InP nanowire devices. The mechanical stability was sufficient to collect scanning XRD and XRF maps with a 50 nm diameter focus. The dark noise of the current measurement system was about 3 fA, which allowed fly scan measurements of X-ray beam induced current (XBIC) in single nanowire devices.

Keywords: X-ray beam induced current (XBIC); scanning X-ray diffraction (XRD); nanowire

---

1. Introduction

X-rays have a long penetration depth compared with electron and optical beams [1], and modern X-ray optics can provide nanofocusing at the range of tens of nanometers [2,3]. This development has made it possible to investigate complete single semiconductor nanostructures [4–11]. By combining the nanofocused X-ray probe with an applied electrical bias as well as electrical current detection, nanodevices can be investigated in more or less realistic operational conditions. In such investigations, the X-rays can be used as a pump, that is, as excitation source with the electrical measurements as a probe, or vice versa.

As an excitation source, X-rays can be used to locally excite charge carriers in semiconductor materials, and if an electrical current is measured, the technique is called X-ray beam induced current (XBIC). The excitation process is similar to that achieved using visible light and electron beams, and XBIC is therefore similar to scanning photocurrent microscopy (SPCM) [12] and electron beam induced current (EBIC) [13]. X-rays have the benefits of a smaller focused beam than laser light and a longer penetration depth than electron beams. Therefore, XBIC could help developing the next-generation nanometer scale electronic devices.

Conversely, an electrical bias can be applied on a nanodevice, with X-rays as a probe. In particular, X-ray diffraction (XRD) can be used to quantify electric-field induced changes in single nanodevices [14–17]. XRD is in principle able to characterize any changes that couple to the crystal lattice, such a piezoelectricity and heating. While the spatial resolution of regular scanning XRD is limited by the focus size, phase retrieval techniques can overcome this limitation [18,19].

In this article, we will describe a system for combining electrical bias and measurements with nanofocused X-ray methods. The setup has been implemented and tested at the NanoMAX beamline [20] at the new synchrotron source, MAX IV, in Lund, Sweden [21], but it can easily be moved to other synchrotrons. To shed light on the detected electrical signal from the studied devices, the internal noise of this measurement system was studied. We also demonstrate multimode imaging using simultaneous STXM, XRF, XBIC, and scanning XRD from single nanowire devices.

The devices we have studied are based on semiconductor nanowires, but the system is applicable to other nanostructured semiconductor devices. Semiconductor nanowires have been studied for decades due to their promising properties that could overcome limitations in devices based on bulk materials in terms of efficiency, cost and performance. For instance, nanowires have been developed for transistors [22], light emitting diodes (LED), lasers, and solar cells [23].

In STXM, the attenuated and scattered X-rays from the sample are collected while the sample is scanned through a focused X-ray beam. Several imaging contrast modes can be extracted from the transmitted beam, such as absorption contrast from the bright field, the deflected beam in the dark field, and the differential phase contrast (DPC) [24]. The spatial resolution of this imaging technique is limited to the size of the X-ray beam. By overlapping the beam while scanning the sample and having the detector in the far-field region, phase retrieval techniques such as ptychography can be employed to overcome the resolution limit of the focus size [25]. Although ptychography is out of the scope of this article, the described system is fully compatible with this method.

The XBIC signal is generated upon X-ray absorption at the atomic level which as a result excites an inner core electron of an atom as a photoelectron leaving behind a vacant state, called a core hole. A relaxation of higher states, to fill up this vacant state, will emit the excess energy in the form of another X-ray photon called X-ray fluorescence (XRF) emission or an excitation of an Auger electron. In case of semiconductor materials, this secondary electrons and photons can excite further electrons in a cascade process. Eventually, the excited charges will be thermalized to the band edge of the semiconductor. At this point, the charge carriers at the band edge can be collected through the well-known semiconductor carrier transport and recombination processes [26–28].

Unlike scanning XRD, which has been frequently used to study nanowires [15,17,19,29–35], there have only been a few examples of nanowire devices studied using XBIC [8,9,11,36]. XBIC has been employed for studying solar cells since the early 2000s [37,38], when it was mostly used to examine grain boundaries and precipitated metal in polycrystalline silicon for solar cells at micrometer resolution [39–41]. With the recent development of nanofocused X-ray beams [2,3], XBIC has lately been used to study planar solar cells, made of materials such as $Cu(In_{(1-x)}Ga_x)Se_2$ (CIGS), or perovskites, both at nanoscale resolution [42,43].

2. Methods

A photograph of the installed sample holder and a schematic of the experimental setup are shown in Figure 1a,b, respectively. There are specific requirements for a system for combining electrical bias and measurements with nanofocused X-ray techniques. Nanofocusing beamlines such as NanoMAX put some physical constraints on the sample holder. The optics have short focal lengths, which limits the available space. At NanoMAX, the useful working distance is on the order of cm, as shown in Figure 1a, and emerging sub-10 nm focusing optics often have focal depths of about 1 mm [44,45]. Since the sample holder is mounted on a high-precision piezo-motor stage, it needs to be lightweight, as well as mechanically stable and free from induced vibrations. The sample holder must have a hole that transmits both the direct beam, for STXM, and Bragg diffraction, for XRD. The sample holder needs to be able to scale the electrical connections from the electronics to the devices and it must be easy to change the sample as well as the active device on the sample. Finally, to be able to measure the electrical current in single nanodevices, the noise must be minimized.

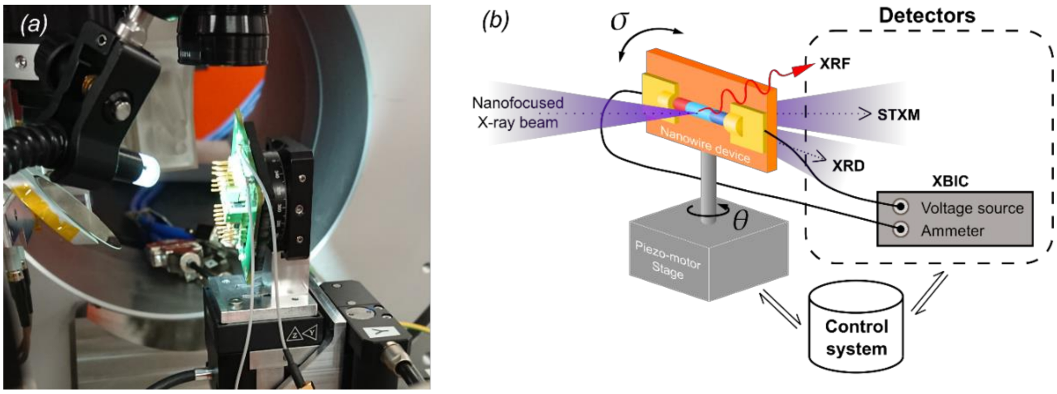

Figure 1. (**a**) Photograph of the installed sample holder on the piezo-motor stage at the NanoMAX beamline. A secured sample on the sample holder is installed on the piezo-motor stage. The tilted mirror to the left of the sample is the 45-degree mirror for the downstream optical microscope used to locate a particular nanowire device on the sample. (**b**) Schematic of the experimental setup at the end-station of NanoMAX. The sample was mounted on the piezo-motor stage, which can be moved in three dimensions and rotated about the vertical axis with the angle θ. Four measurement modes, X-ray fluorescence (XRF), Scanning transmission X-ray microscopy (STXM), X-ray diffraction (XRD), and X-ray beam induced current (XBIC), are available with this setup at NanoMAX. All the detectors as well as the piezo-motor stage are managed by the control-system.

The sample holder for the measurement, fulfilling the aforementioned requirements, is shown in Figure 2a. This sample holder consists of two main parts. First, there is a printed circuit board (PCB), which has a 16-pin chip socket, vertical pin connectors, and U.FL coaxial terminals (Figure 2b). The chip socket uses the well-established DIP format. Each sample chip is mounted and wire bonded to a DIP chip carrier, the white part in Figure 2b, before the experiment. The standard format makes it easy to change samples and to investigate different types of devices. Each slot of the chip socket is directly connected to a pin in a set of three vertical pins, where the two other pins are connected to different U.FL coaxial terminals on the circuit board (Figure S2b in Supplementary Materials). The active device on the chip is selected by connecting these pins. Each device is normally connected with two connections, although up to four can be used (e.g., for transistor gates). Each pin is connected to the voltage supply source on one end and the amperemeter on the other end, with U.FL coaxial connectors (gray cable in Figure 1a). This mini-coaxial connector, which allows a coaxial connection all the way from the PCB to the electronics, replaced pin connectors used in our previous sample holder design (Figure S2a). Please note that each U.FL connection is available on opposite sides of the PCB, since space constraints often makes one side impossible to reach.

The second part of the sample holder is the rotation mount (*Thorlabs CRM1/M*, Figure 2a) to which the circuit board is mounted. This allows the sample to be rotated around the optical axis with angle σ, such that the nanowire device can be manually aligned in vertical or horizontal, as shown in Figure 1b. This makes it easy to make one-dimensional scans along the nanowire axis. For XRD experiments, the manual rotation makes it possible to align the scattering plane in a favorable direction, without needing an extra goniometer rotation axis. The rotation mount is attached to an aluminum adapter plate, which is custom made to fit the top of the piezo motor.

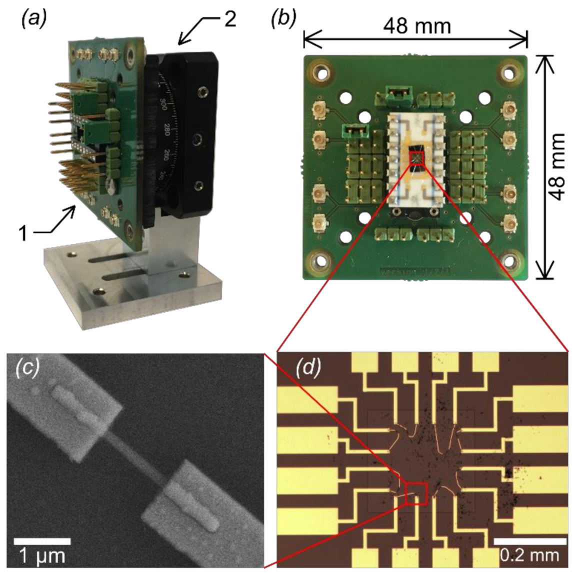

Figure 2. Nanowire device on the chip carrier and sample holder (**a**) The two main components of the sample holder are (1) the circuit board (green) and (2) the rotational mount (black). (**b**) The front side of the circuit board mounted with the 10 × 18 mm 14-pin chip carrier which has the nanowire device on the top. The circuit board consists of a 16-pin chip socket, vertical pins and U.FL terminals. This circuit board size is 48 × 48 mm. This side faces upstream towards the X-ray beam. Each slot of the chip socket is connected to a pin in a set of three vertical pins. By selecting pins, a particular nanowire device can be connected to the external equipment. (**c**) SEM image of the contacted single nanowire device. (**d**) Microscope image of eight nanowire devices on a SiN membrane window, seen as a lighter square in the center, surrounded by Au bonding pads which was attached on the chip carrier in (**b**).

For the electrical bias and current measurements, we integrated the amperemeter, *Keysight B2985A*, into the control system. This amperemeter has a built-in voltage source and is used to collect the XBIC signal from the sample.

The X-rays in the experiment were generated by MAX IV (Lund, Sweden), which is the first fourth-generation synchrotron radiation source [21]. The NanoMAX beamline [20] uses a Kirkpatrick-Baez (KB) mirror pair to focus the X-rays down to about 50 nm. In this experiment, the energy of the beam was 15 keV. The sample holder was mounted on a piezo-motor stage, which can be scanned in all three directions. The two-axis goniometer can rotate the sample for X-ray diffraction experiments (Figure 1b). The available detectors at the end-station for this experiment were (1) *Pilatus 100K* for the transmission beam (2) *Merlin quad*, 2 × 2 Medipix chip, mounted on the robot arm for the Bragg diffraction, and (3) *Amptek XR-100 silicon drift detector* for the XRF emission from the sample (Figure 1b). All these components at the end station are operated by the TANGO-based control system [46].

Scanning measurements are traditionally performed step-by-step, allowing the motors to stop at each position before the data acquisition. With the high flux at beamlines such as NanoMAX, acquisition times of only 10–100 ms are typically necessary. The measurement time in a step scan is then dominated by an overhead from starting, stopping, and reading out the motor positions. To reduce this overhead, the control system at NanoMAX can employ “fly-scan”, where the sample is continuously moving. This is not only much more efficient, but can lead to less sample drift and therefore, somewhat counter-intuitively, improved spatial resolution. While the stage motor is sweeping in the fast scan direction, the photon detectors are triggered by the control system [46]. In a typical step-by-step scan, the collected XBIC signal is read out with every step, but this is too slow for the fly-scan measurements. Instead, we connected the analog voltage output of the amperemeter to a voltage to frequency converter, which in turn was connected to the control system.

The tested nanodevice was a horizontal contacted single nanowire device with a *p-i-n* doped InP nanowire (Figure 2c,d). A similar type of nanowires has been developed for the next generation solar cells [23], which have already been thoroughly studied using nano-XBIC and XRF in our previous works [10,11]. These nanowire devices were fabricated on a 0.25 × 0.25 mm Si_3N_4 membrane window on a 3 × 5 mm Si chip from *Silson* (Southam, Warwickshire, England). The chip was glued and wire bonded to a 10 × 18 mm 14-pin DIP chip carrier and secured on the sample holder as shown in Figure 2b. More details regarding the nanowire device can be found in the supporting information.

3. Results and Discussion

First, we investigated the internal electrical noise by measuring the background current of the nanowire device without an X-ray beam under dark conditions [47]. No applied bias was used. Three measured current ranges of the amperemeter were tested, namely 2 pA, 20 pA, and 200 pA. We expected that the operation of the piezo motors in the sample stage could induce noise during the measurement. Therefore, the experiment was done with and without moving piezo motors.

Figure 3 displays some of the results from the internal noise of the XBIC measurement system. The current in the nanowire device as a function of time, without moving the piezo motor, is displayed in Figure 3a for each of the three used current ranges of the amperemeter. The offsets between each measurement at different current ranges were affected by the accuracy of the amperemeter as mentioned in the data sheet of the equipment. We plotted these measurements as histograms, as shown in Figure 3b, and used the standard deviation (SD) to estimate the noise level. Figure 3b is a comparison of the new and the old sample holder with the U.FL coaxial terminal and pin terminal, respectively. The extracted SDs at different tested conditions are plotted in Figure 3c.

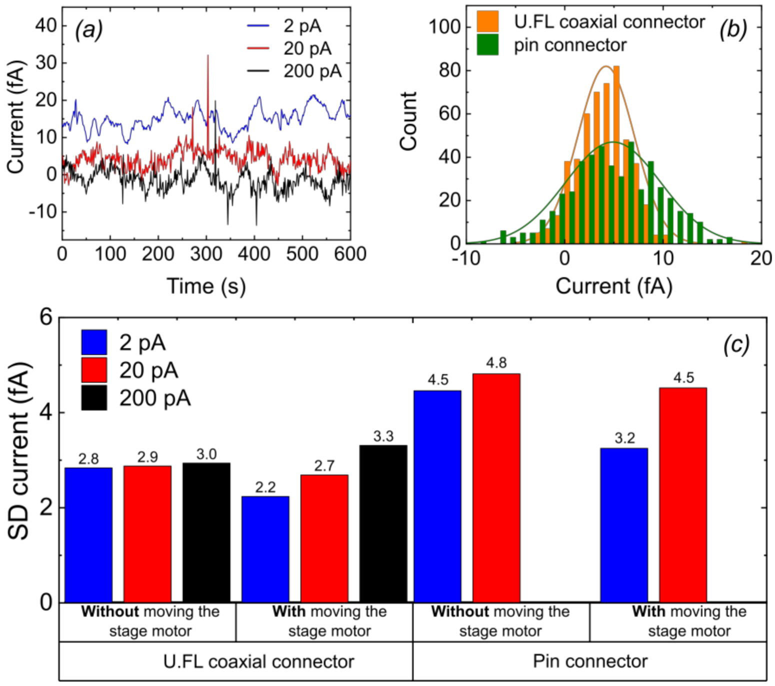

Figure 3. Internal noise of the XBIC measurement system. (**a**) The current through the nanowire device measured at 2 pA (blue trace), 20 pA (red trace) and 200 pA (black trace) current range of the amperemeter as a function of time. (**b**) The same measured current as (**a**) with a different sample holder design, that is, with U.FL connector (orange) and pin connector (green) as a terminal, plotted as a histogram exhibiting a normal distribution with fitting curve. These measurements were done at a 20 pA current range. (**c**) The standard deviation (SD) of the measured current at different measurement conditions.

The noise level calculated from the SD of the measurement indicated that there was only ~2% difference between each measurement range as represented in Figure 3c. With the operating stage motor, the measured spread in noise levels increased. However, none of these shifts could be considered statistically significant.

When we compared the old design of sample holder with the pin terminals, the SD of the old sample holder was consistently about ~35% higher at every measurement condition (Figure 3b,c). Apart from the improved noise level, measured data points with a non-repeatable spike (Figure S3), which occurred frequently using the old design in our previous XBIC experiment [9], were also reduced.

Finally, we investigated the effect of ambient room light, which resulted in a substantial photocurrent of around 25 fA (Figure S4). The noise level only changed marginally. Please note that applying light for the inline microscope leads to strong photocurrents (not shown), comparable in magnitude to the XBIC signal.

From these results, we can state that the dark noise in the measurement system is only about 3 fA, that is ~2×10^4 electrons per second, at these conditions. Please note that we did not employ any X-ray chopper, or any electrical shielding of the PCB. We did not observe any increase in noise from scanning with the piezo motors. The small device size, with an active depletion region volume of less than one μm^3, is probably a main reason for these very low noise levels.

Next, we demonstrate a two-dimensional fly-scan simultaneously mapping STXM, XRF, and XBIC of the nanowire device in Figure 4. The edge of the nanowire device distinguishing the nanowire from the metal contact can be seen from the DPC image of the detected STXM in Figure 4a. The DPC image is calculated as the radial magnitude of the vertical and horizontal DPCs. The XRF map in Figure 4b shows the relatively weak In L signal from the InP nanowire and the stronger Au L emission from the metal contacts. We can also observe the nanowire's Au seed particle beneath the metal contact (Figure 4a,b). Finally, the XBIC map is shown in Figure 4c.

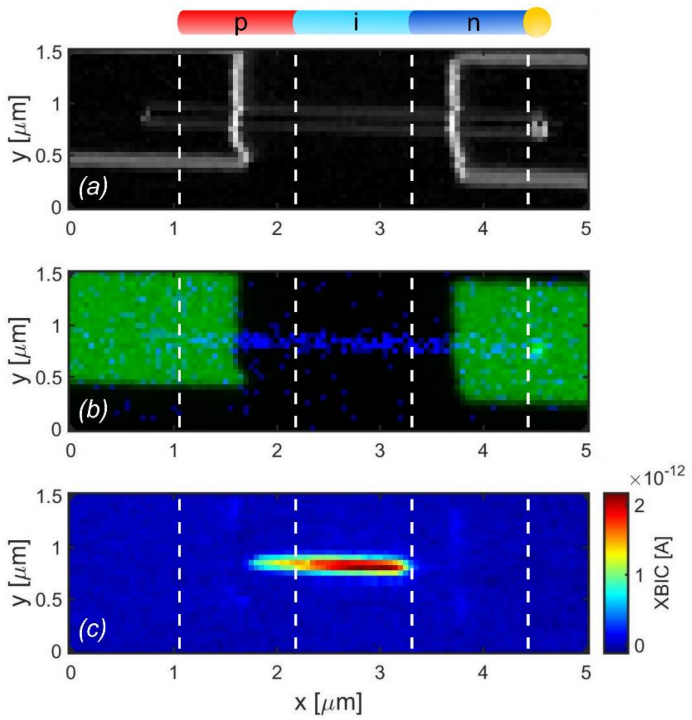

Figure 4. Multimodal imaging of a nanowire device. (**a**) Differential phase contrast (DPC) image of STXM showing the edges of the nanowire and metal contacts. (**b**) Material composition of the nanowire device, where the blue area and the green area are from XRF emission of In and Au atoms, respectively. (**c**) Color map of the XBIC signal from the nanowire device. The step length of this scan is 50 nm in both x- and y-direction with an acquisition time of 0.1 s and a latency time of 0.01 s for this fly-scan measurement. Dashed lines in these figures indicate the nominal position of each segment with the length of 1.1 μm using the Au particle observed in (**a**) and (**b**) as a reference position. Due to variations in the nanowire growth process, the actual length of this nanowire was slightly longer than the nominal one.

The XBIC map in Figure 4c sheds light on the underlying carrier collection mechanism of the nanowire device [11,48]. The signal is generated in the middle segment, approximately corresponding to the depletion region of the solar cell. After excitation, the electrons need an electric field to generate a net current, and such a field is only present in the depletion region. The signal is also affected by carrier recombination, which will be affected by doping, surface states and other recombination centers. This makes XBIC a versatile tool for investigating carrier dynamics and carrier collection in nanostructures.

With the information from the XRF map, we could investigate the material composition and doping concentration within nanowires as demonstrated by Johannes et al. [8] and Troian et al. [10]. The asymmetry of the XBIC profile in this map, with a long gradient at the left slope and a sharp one at the right slope, could be explained using the XRF map of the doping concentration as discussed in our previous work [11]. However, scanning XRF with sufficient sensitivity to measure the doping concentration requires a very high photon flux, which could affect the charge collection of the nanowire device monitored with XBIC or even damage the device. Therefore, the X-ray photon flux in this experiment was attenuated to be $\Phi \approx 5.7 \times 10^8$ s^{-1}, which is equivalent to the excitation level of 1 sun illumination as discussed in our previous work [11,49].

The yield of the photogenerated charges, η, contributing to the XBIC signal is the ratio between the X-ray photon energy and the ionization energy of the semiconductor, $\eta = E/\varepsilon$ [50]. With the X-ray energy in the order of keV, η can be several thousand in the XBIC process. The absorbed X-ray photon flux of the material at thickness, z, is quantified by the X-ray absorption probability, p_{abs}, which is the ratio between the absorbed and the incident X-ray photon flux. The absorption probability can be calculated from Beer–Lambert's law with knowledge of the X-ray absorption coefficient. This means that p_{abs} depends on the material composition and geometry as well as the X-ray energy. With these parameters, η and p_{abs}, the theoretical maximum XBIC signal can be calculated by $I_{XBIC} = q\eta p_{abs}\Phi$, where q is the charge constant and Φ is the incident X-ray photon flux. In this experiment, the yield of the photogenerated charges, η, and the X-ray absorption probability, p_{abs}, of the *p-i-n* doped InP nanowire were calculated to be $\eta = 3.5 \times 10^3$ and $p_{abs} = 0.003$, respectively. With the X-ray photon flux of $\Phi \approx 5.7 \times 10^8$ s^{-1}, the theoretical maximum XBIC signal is $I_{XBIC} = 9.7 \times 10^{-10}$ A. In contrast, the maximum measured XBIC from the nanowire device was 2.46×10^{-12} A. The difference between the measurement and the calculation is due to the high escape probability for secondary electrons and photons in these nanostructures [11,48].

Despite these losses, the XBIC signal was about three orders of magnitude higher than the dark current of the nanowire device and the internal noise of the measurement system. In fact, the XBIC showed the strongest contrast of all modes and was used for the sample alignment. Nonetheless, it is important to have enough latency time for the amperemeter to stabilize, since otherwise the measurement result is affected by the frequency of the triggering period (Figure S5). There is a slight distortion of the image, seen as a bent vertical edge of the metal contact, which is caused by drift in the scanning stage.

The scanning XRD results of a second device on the same chip are shown in Figure 5. Prior to the scanning XRD measurement, the nanowire device was aligned at the center of rotation of the motor stage. However, we still observed non-systematic real-space movement of the sample between different rotations in the XRF maps (Figure 5a). The XRF maps were then used to correct the position of the sample for each rotation angle, θ, before the reciprocal space mapping. The X-ray photon flux was increased to $\Phi \approx 1.4{\times}10^9$ s^{-1} for this measurement in order to get the Bragg diffraction with a considerable intensity. The total intensity of the Bragg diffraction is displayed in Figure 5b. A low-intensity region is observed around $x = 1.2$ µm, which is due to the very large tilt (bending) which put the nanowire lattice out of the angular range.

Reciprocal space mapping using the center of mass of the Bragg peak was used to generate a strain map (Figure 5c) as well as two tilt maps (Figure 5d,e), where α and β correspond to the tilt around the optical axis and the tilt around the vertical axis, respectively. The nanowire is strained, presumably due to stress from the metal contacts. The total range of the strain variation is about 0.1%, but we can distinguish variations on the order of 0.01% (10^{-4}). The minimum strain variation that could be resolved in such a measurement is not trivial to quantify, but similar investigations have imaged strain variation of less than 10^{-5} [51]. Please note that the strain here (i.e., the change on average lattice plane distance) can also be affected by the doping profile and stacking faults.

The strong tilts are due to bending of the nanowire, which is induced by the metal contacts on both ends of the nanowire [15,17]. The shape of the nanowire can be reconstructed using a line integral [52], although such an analysis is outside of the scope of the present article. The nanowire here bends out in an arch above the substrate, similar to devices previously reported [15].

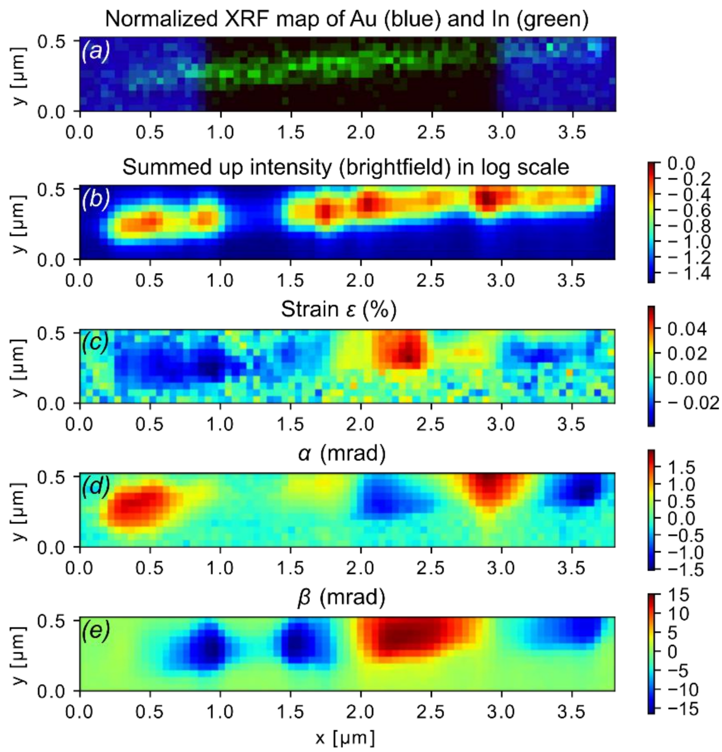

Figure 5. Scanning XRD of a single nanowire device (similar but not identical to the device in Figure 4): (**a**) XRF map, showing Au (blue) and In (green), (**b**) total intensity of the Bragg peaks (**c**) strain, in %, (**d**) lattice tilt around the optical axis, (**e**) lattice tilt around the vertical axis.

4. Conclusions

We have presented a system for combining nanofocused X-rays with electrical measurements at the NanoMAX beamline. The current from the tested sample can be directly collected, due to the low noise (~3 fA) which allows operando experiments simultaneously combining STXM, XRF, scanning XRD, and XBIC. In this way, information about morphology, elemental composition, crystal structure, and charge collection can be correlated. The system expands the capability of NanoMAX, by adding a new contrast mode, XBIC, that can be used to investigate carrier collection and carrier dynamics in nanostructured devices. Furthermore, it opens up the possibility to combine the established techniques at NanoMAX with an electric bias. For instance, it would be possible to study the strain and the shape of the nanowire as function of applied electric bias [15]. While we have demonstrated the system for a particular system, single nanowires, it should be useful for any devices where electrical bias or current collection is used, for instance transistors, batteries, light emitting diodes, or electrochemical devices.

Supplementary Materials: The following are available online at http://www.mdpi.com/2073-4352/9/8/432/s1, Figure S1: An image of horizontal contacted single nanowire device, Figure S2: An old designed sample holder and a schematic diagram of the circuit board, Figure S3: Internal noise of the measurement system using the old designed sample holder, Figure S4: Comparison noises with and without an ambient light, Figure S5: XBIC map using “fly-scan” with too short latency time.

Author Contributions: Conceptualization, J.W. and L.C.; methodology, J.W., A.B. and L.C.; software, J.W., S.H. and L.C.; validation, J.W. and A.B.; formal analysis, L.C. and S.H.; investigation, J.W., S.H., L.C. and H.D.; resources, A.B., G.O. and M.T.B.; data curation, L.C.; writing—original draft preparation, L.C..; writing—review and editing, J.W.; visualization, L.C.; supervision, J.W.; project administration, J.W.; funding acquisition, J.W.

Funding: This research was funded by the Röntgen-Ångström Cluster, NanoLund, Marie Sklodowska Curie Actions, Cofund, Project INCA 600398, and the Swedish Research Council grant number 2015-00331.

Acknowledgments: The support from the beamline staff is greatly acknowledged. The MAX IV Laboratory receives funding through the Swedish Research Council under grant no 2013-02235.

Conflicts of Interest: The authors declare no conflict of interest.

References

1. Stuckelberger, M.; West, B.; Husein, S.; Guthrey, H.; Al-Jassim, M.; Chakraborty, R.; Buonassisi, T.; Maser, J.M.; Lai, B.; Stripe, B. Latest developments in the x-ray-*based* characterization of thin-film solar cells. In Proceedings of the Photovoltaic Specialist Conference (PVSC), New Orleans, LA, USA, 14–19 June 2015; pp. 1–6.
2. Mimura, H.; Handa, S.; Kimura, T.; Yumoto, H.; Yamakawa, D.; Yokoyama, H.; Matsuyama, S.; Inagaki, K.; Yamamura, K.; Sano, Y.; et al. Breaking the 10-nm barrier in hard-X-ray focusing. *Nat. Phys.* **2010**, *6*, 122–125. [CrossRef]
3. Döring, F.; Robisch, A.L.; Eberl, C.; Osterhoff, M.; Ruhlandt, A.; Liese, T.; Schlenkrich, F.; Hoffmann, S.; Bartels, M.; Salditt, T.; et al. Sub-5 nm hard x-ray point focusing by a combined Kirkpatrick-Baez mirror and multilayer zone plate. *Opt. Express* **2013**, *21*, 19311–19323.
4. Holt, M.; Harder, R.; Winarski, R.; Rose, V. Nanoscale Hard X-Ray Microscopy Methods for Materials Studies. *Annu. Rev. Mater. Res.* **2013**, *43*, 183–211. [CrossRef]
5. Etzelstorfer, T.; Sueess, M.J.; Schiefler, G.L.; Jacques, V.L.; Carbone, D.; Chrastina, D.; Isella, G.; Spolenak, R.; Stangl, J.; Sigg, H. Scanning X-ray strain microscopy of inhomogeneously strained Ge micro-bridges. *J. Synchrotron Radiat.* **2014**, *21*, 111–118. [CrossRef]
6. Ulvestad, A.; Singer, A.; Cho, H.-M.; Clark, J.N.; Harder, R.; Maser, J.; Meng, Y.S.; Shpyrko, O.G. Single Particle Nanomechanics in Operando Batteries via Lensless Strain Mapping. *Nano Lett.* **2014**, *14*, 5123–5127. [CrossRef]
7. Davtyan, A.; Lehmann, S.; Kriegner, D.; Zamani, R.R.; Dick, K.A.; Bahrami, D.; Al-Hassan, A.; Leake, S.J.; Pietsch, U.; Holý, V. Characterization of individual stacking faults in a wurtzite GaAs nanowire by nanobeam X-ray diffraction. *J. Synchrotron Radiat.* **2017**, *24*, 981–990. [CrossRef]
8. Johannes, A.; Salomon, D.; Martinez-Criado, G.; Glaser, M.; Lugstein, A.; Ronning, C. In operando x-ray imaging of nanoscale devices: Composition, valence, and internal electrical fields. *Sci. Adv.* **2017**, *3*, eaao4044. [CrossRef]
9. Chayanun, L.; Dagytė, V.; Troian, A.; Salomon, D.; Borgström, M.T.; Wallentin, J. Spectrally resolved x-ray beam induced current in a single InGaP nanowire. *Nanotechnology* **2018**, *29*, 454001. [CrossRef]
10. Troian, A.; Otnes, G.; Zeng, X.; Chayanun, L.; Dagytė, V.; Hammarberg, S.; Salomon, D.; Timm, R.; Mikkelsen, A.; Borgström, M.T.; et al. Nanobeam X-ray Fluorescence Dopant Mapping Reveals Dynamics of in Situ Zn-Doping in Nanowires. *Nano Lett.* **2018**, *18*, 6461–6468. [CrossRef]
11. Chayanun, L.; Otnes, G.; Troian, A.; Hammarberg, S.; Salomon, D.; Borgström, M.T.; Wallentin, J. Nanoscale mapping of carrier collection in single nanowire solar cells using X-ray beam induced current. *J. Synchrotron Radiat.* **2019**, *26*, 102–108. [CrossRef]
12. Ahn, Y.H.; Tsen, A.W.; Kim, B.; Park, Y.W.; Park, J. Photocurrent Imaging of p−n Junctions in Ambipolar Carbon Nanotube Transistors. *Nano Lett.* **2007**, *7*, 3320–3323. [CrossRef] [PubMed]
13. Hanoka, J.I. Electron-beam-induced current characterization of polycrystalline silicon solar cells. *Sol. Cells* **1980**, *1*, 123–139. [CrossRef]
14. Ulvestad, A.; Singer, A.; Clark, J.N.; Cho, H.M.; Kim, J.W.; Harder, R.; Maser, J.; Meng, Y.S.; Shpyrko, O.G. Topological defect dynamics in operando battery nanoparticles. *Science* **2015**, *348*, 1344–1347. [CrossRef] [PubMed]
15. Wallentin, J.; Osterhoff, M.; Salditt, T. In Operando X-Ray Nanodiffraction Reveals Electrically Induced Bending and Lattice Contraction in a Single Nanowire Device. *Adv. Mater.* **2016**, *28*, 1788–1792. [CrossRef] [PubMed]

16. Karpov, D.; Liu, Z.; Rolo, T.d.S.; Harder, R.; Balachandran, P.V.; Xue, D.; Lookman, T.; Fohtung, E. Three-dimensional imaging of vortex structure in a ferroelectric nanoparticle driven by an electric field. *Nat. Commun.* **2017**, *8*, 280. [CrossRef]
17. Lazarev, S.; Dzhigaev, D.; Bi, Z.; Nowzari, A.; Kim, Y.Y.; Rose, M.; Zaluzhnyy, I.A.; Gorobtsov, O.Y.; Zozulya, A.V.; Lenrick, F.; et al. Structural Changes in a Single GaN Nanowire under Applied Voltage Bias. *Nano Lett.* **2018**, *18*, 5446–5452. [CrossRef]
18. Godard, P.; Carbone, G.; Allain, M.; Mastropietro, F.; Chen, G.; Capello, L.; Diaz, A.; Metzger, T.H.; Stangl, J.; Chamard, V. Three-dimensional high-resolution quantitative microscopy of extended crystals. *Nat. Commun.* **2011**, *2*, 568. [CrossRef]
19. Hill, M.O.; Calvo-Almazan, I.; Allain, M.; Holt, M.V.; Ulvestad, A.; Treu, J.; Koblmüller, G.; Huang, C.; Huang, X.; Yan, H.; et al. Measuring Three-Dimensional Strain and Structural Defects in a Single InGaAs Nanowire Using Coherent X-ray Multiangle Bragg Projection Ptychography. *Nano Lett.* **2018**, *18*, 811–819. [CrossRef]
20. Johansson, U.; Vogt, U.; Mikkelsen, A. NanoMAX: A hard x-ray nanoprobe beamline at MAX IV. *SPIE* **2013**, *8851*, 88510L.
21. Eriksson, M.; Malmgren, L.; Al-Dmour, E.; Thorin, S.; Johansson, M.; Leemann, S.; Andersson, Å; Tavares, P. Commissioning of the MAX IV light source. In Proceedings of the IPAC 2016, Busan, Korea, 8–13 May 2016.
22. Memisevic, E.; Hellenbrand, M.; Lind, E.; Persson, A.R.; Sant, S.; Schenk, A.; Svensson, J.; Wallenberg, R.; Wernersson, L.-E. Individual Defects in InAs/InGaAsSb/GaSb Nanowire Tunnel Field-Effect Transistors Operating below 60 mV/decade. *Nano Lett.* **2017**, *17*, 4373–4380. [CrossRef]
23. Otnes, G.; Barrigón, E.; Sundvall, C.; Svensson, K.E.; Heurlin, M.; Siefer, G.; Samuelson, L.; Åberg, I.; Borgström, M.T. Understanding InP Nanowire Array Solar Cell Performance by Nanoprobe-Enabled Single Nanowire Measurements. *Nano Lett.* **2018**, *18*, 3038–3046. [CrossRef] [PubMed]
24. Bunk, O.; Bech, M.; Jensen, T.H.; Feidenhans'l, R.; Binderup, T.; Menzel, A.; Pfeiffer, F. Multimodal x-ray scatter imaging. *New J. Phys.* **2009**, *11*, 123016. [CrossRef]
25. Rodenburg, J.M. Ptychography and Related Diffractive Imaging Methods. *Adv. Imaging Electron Phys.* **2008**, *150*, 87–184.
26. Rodnyi, P.A. *Physical Processes in Inorganic Scintillators*; CRC press: Boca Raton, FL, USA, 1997.
27. Nikl, M. Scintillation detectors for x-rays. *Meas. Sci. Technol.* **2006**, *17*, R37–R54. [CrossRef]
28. Lecoq, P.; Gektin, A.; Korzhik, M. *Inorganic Scintillators for Detector Systems: Physical Principles and Crystal Engineering*; Springer: Berlin/Heidelberg, Germany, 2016.
29. Eymery, J.; Rieutord, F.; Favre-Nicolin, V.; Robach, O.; Niquet, Y.-M.; Fröberg, L.; Mårtensson, T.; Samuelson, L. Strain and Shape of Epitaxial InAs/InP Nanowire Superlattice Measured by Grazing Incidence X-ray Techniques. *Nano Lett.* **2007**, *7*, 2596–2601. [CrossRef] [PubMed]
30. Diaz, A.; Mocuta, C.; Stangl, J.; Mandl, B.; David, C.; Vila-Comamala, J.; Chamard, V.; Metzger, T.H.; Bauer, G. Coherent diffraction imaging of a single epitaxial InAs nanowire using a focused x-ray beam. *Phys. Rev. B* **2009**, *79*, 125324. [CrossRef]
31. Newton, M.C.; Leake, S.J.; Harder, R.; Robinson, I.K. Three-dimensional imaging of strain in a single ZnO nanorod. *Nat. Mater.* **2009**, *9*, 120. [CrossRef]
32. Favre-Nicolin, V.; Mastropietro, F.; Eymery, J.; Camacho, D.; Niquet, Y.M.; Borg, B.M.; Messing, M.E.; Wernersson, L.E.; Algra, R.E.; Bakkers, E.P.A.M.; et al. Analysis of strain and stacking faults in single nanowires using Bragg coherent diffraction imaging. *New J. Phys.* **2010**, *12*, 035013. [CrossRef]
33. Haag, S.T.; Richard, M.-I.; Welzel, U.; Favre-Nicolin, V.; Balmes, O.; Richter, G.; Mittemeijer, E.J.; Thomas, O. Concentration and Strain Fields inside a Ag/Au Core–Shell Nanowire Studied by Coherent X-ray Diffraction. *Nano Lett.* **2013**, *13*, 1883–1889. [CrossRef]
34. Stankevič, T.; Mickevičius, S.; Schou Nielsen, M.; Kryliouk, O.; Ciechonski, R.; Vescovi, G.; Bi, Z.; Mikkelsen, A.; Samuelson, L.; Gundlach, C. Measurement of strain in InGaN/GaN nanowires and nanopyramids. *J. Appl. Crystallogr.* **2015**, *48*, 344–349. [CrossRef]
35. Schroth, P.; Jakob, J.; Feigl, L.; Mostafavi Kashani, S.M.; Vogel, J.; Strempfer, J.; Keller, T.F.; Pietsch, U.; Baumbach, T. Radial Growth of Self-Catalyzed GaAs Nanowires and the Evolution of the Liquid Ga-Droplet Studied by Time-Resolved in Situ X-ray Diffraction. *Nano Lett.* **2018**, *18*, 101–108. [CrossRef] [PubMed]
36. Wallentin, J.; Osterhoff, M.; Wilke, R.N.; Persson, K.-M.; Wernersson, L.-E.; Sprung, M.; Salditt, T. Hard X-ray Detection Using a Single 100 nm Diameter Nanowire. *Nano Lett.* **2014**, *14*, 7071–7076. [CrossRef] [PubMed]

37. Hieslmair, H.; Istratov, A.A.; Sachdeva, R.; Weber, E.R. *New Synchrotron-Radiation-Based Technique to Study Localized Defects in Silicon: 'EBIC' with X-ray Excitation*; LBNL/ALS–43453; Ernest Orlando Lawrence Berkeley National Lab.: Berkeley, CA, USA, 2000; Available online: https://inis.iaea.org/search/search.aspx?orig_q=RN:33061273 (accessed on 15 August 2019).
38. Vyvenko, O.F.; Buonassisi, T.; Istratov, A.A.; Weber, E.R. X-ray beam induced current/microprobe x-ray fluorescence: Synchrotron radiation-*based* x-ray microprobe techniques for analysis of the recombination activity and chemical nature of metal impurities in silicon. *J. Phys. Condens. Matter* **2004**, *16*, S141. [CrossRef]
39. Buonassisi, T.; Heuer, M.; Vyvenko, O.F.; Istratov, A.A.; Weber, E.R.; Cai, Z.; Lai, B.; Ciszek, T.F.; Schindler, R. Applications of synchrotron radiation X-ray techniques on the analysis of the behavior of transition metals in solar cells and single-crystalline silicon with extended defects. *Phys. B: Condens. Matter* **2003**, *340–342*, 1137–1141. [CrossRef]
40. Buonassisi, T.; Istratov, A.A.; Pickett, M.D.; Marcus, M.A.; Hahn, G.; Riepe, S.; Isenberg, J.; Warta, W.; Willeke, G.; Ciszek, T.F.; et al. Quantifying the effect of metal-rich precipitates on minority carrier diffusion length in multicrystalline silicon using synchrotron-based spectrally resolved x-ray beam-induced current. *Appl. Phys. Lett.* **2005**, *87*, 044101. [CrossRef]
41. Seifert, W.; Vyvenko, O.; Arguirov, T.; Kittler, M.; Salome, M.; Seibt, M.; Trushin, M. Synchrotron-based investigation of iron precipitation in multicrystalline silicon. *Superlattices Microstruct.* **2009**, *45*, 168–176. [CrossRef]
42. West, B.; Husein, S.; Stuckelberger, M.; Lai, B.; Maser, J.; Stripe, B.; Rose, V.; Guthrey, H.; Al-Jassim, M.; Bertoni, M. Correlation between grain composition and charge carrier collection in Cu(In,Ga)Se2 solar cells. In Proceedings of the 2015 IEEE 42nd Photovoltaic Specialist Conference (PVSC), New Orleans, LA, USA, 14–19 June 2015; pp. 1–4.
43. Stuckelberger, M.; Nietzold, T.; Hall, G.N.; West, B.; Werner, J.; Niesen, B.; Ballif, C.; Rose, V.; Fenning, D.P.; Bertoni, M.I. Elemental distribution and charge collection at the nanoscale on perovskite solar cells. In Proceedings of the 2016 IEEE 43rd Photovoltaic Specialists Conference (PVSC), Portland, OR, USA, 5–10 June 2016; pp. 1191–1196.
44. Osterhoff, M.; Eberl, C.; Döring, F.; Wilke, R.N.; Wallentin, J.; Krebs, H.-U.; Sprung, M.; Salditt, T. Towards multi-order hard X-ray imaging with multilayer zone plates. *J. Appl. Crystallogr.* **2015**, *48*, 116–124. [CrossRef]
45. Bajt, S.; Prasciolu, M.; Fleckenstein, H.; Domaracký, M.; Chapman, H.N.; Morgan, A.J.; Yefanov, O.; Messerschmidt, M.; Du, Y.; Murray, K.T.; et al. X-ray focusing with efficient high-NA multilayer Laue lenses. *Light: Sci. Amp; Appl.* **2018**, *7*, 17162. [CrossRef]
46. Bell, P.; Hardion, V.; Jamróz, J.; Lidón-Simon, J. Control and Data Acquisition Using TANGO and SARDANA at the Nanomax Beamline at MAX IV. In Proceedings of the 16th International Conference on Accelerator and Large Experimental Control Systems, Barcelona, Spain, 8–13 October 2017; pp. 900–904.
47. Spear, J.D. Shot noise in x-ray measurements with p-i-n diodes. *Rev. Sci. Instrum.* **2005**, *76*, 076101. [CrossRef]
48. Stuckelberger, M.; West, B.; Nietzold, T.; Lai, B.; Maser, J.M.; Rose, V.; Bertoni, M.I. Engineering solar cells *based on* correlative X-ray microscopy. *J. Mater. Res.* **2017**, *32*, 1825–1854. [CrossRef]
49. Yang, C.; Pyry, K.; Mats-Erik, P.; Nicklas, A. Optimization of the short-circuit current in an InP nanowire array solar cell through opto-electronic modeling. *Nanotechnology* **2016**, *27*, 435404.
50. Alig, R.C.; Bloom, S. Secondary-electron-escape probabilities. *J. Appl. Phys.* **1978**, *49*, 3476–3480. [CrossRef]
51. Chahine, G.A.; Richard, M.-I.; Homs-Regojo, R.A.; Tran-Caliste, T.N.; Carbone, D.; Jacques, V.L.R.; Grifone, R.; Boesecke, P.; Katzer, J.; Costina, I.; et al. Imaging of strain and lattice orientation by quick scanning X-ray microscopy combined with three-dimensional reciprocal space mapping. *J. Appl. Crystallogr.* **2014**, *47*, 762–769. [CrossRef]
52. Wallentin, J.; Jacobsson, D.; Osterhoff, M.; Borgström, M.T.; Salditt, T. Bending and Twisting Lattice Tilt in Strained Core–Shell Nanowires Revealed by Nanofocused X-ray Diffraction. *Nano Lett.* **2017**, *17*, 4143–4150. [CrossRef]